Structure and dielectric properties of double A-site doped bismuth sodium titanate relaxor ferroelectrics for high power energy storage applications

Hangfeng Zhang,[1,2] Bin Yang,[3] A. Dominic Fortes,[4] Haixue Yan,[2*] Isaac Abrahams[1*]

[1]School of Biological and Chemical Sciences, Queen Mary University of London, Mile End Road, London E1 4NS, UK.

[2]School of Engineering and Materials Sciences, Queen Mary University of London, Mile End Road, London E1 4NS, UK.

[3]Faculty of Science and Engineering, University of Chester, CH2 4NU, UK

[4]STFC ISIS Facility, Rutherford Appleton Laboratory, Chilton Didcot, Oxfordshire, OX11 OQX, UK.

Corresponding Authors

H. Yan tel: +44 207 882 5164 email: h.x.yan@qmul.ac.uk

I. Abrahams tel: +44 207 882 3235 email: i.abrahams@qmul.ac.uk

Abstract

The structural and dielectric properties of barium/strontium substituted $Bi_{0.5}Na_{0.5}TiO_3$ were examined in compositions of general formula $(Ba_{0.4}Sr_{0.6}TiO_3)_x(Bi_{0.5}Na_{0.5}TiO_3)_{1-x}$. An average classic cubic perovskite structure is maintained from x = 0.5 to 1.0. The temperature dependence of dielectric properties of studied compositions shows relaxor-ferroelectric behaviour attributed to the existence of polar nano-regions. Ferroelectric measurements under variable temperature demonstrated two transitions from normal ferroelectric to relaxor-ferroelectric and relaxor-ferroelectric to paraelectric, at the dipole freezing temperature, T_f, and temperature of maximum permittivity, T_m, respectively. The obtained value of T_f coincides with the onset of linear thermal expansion of the cubic unit cell parameter obtained from high resolution powder neutron diffraction data. Careful analysis of the neutron diffraction data revealed no significant change in the average cubic structure from -263 to 150 °C. However, changes in the Gaussian variance component of the neutron peak shape, reveal three distinct regions with transitions at about -100 and 100 °C corresponding to the beginning and end of the dielectric dispersion seen in the permittivity and loss spectra. This variation in the Gaussian variance parameter is attributed to the activity of the polar nano-regions. The composition $(Ba_{0.4}Sr_{0.6})_{0.5}(Bi_{0.5}Na_{0.5})_{0.5}TiO_3$ was found to exhibit the maximum recoverable energy storage density, with a value of 1.618 J cm^{-3} and 76.9% storage efficiency at a field of 17 kV mm^{-1}.

1. Introduction

The continuing development of renewable energy sources for power generation has led to increased demand for energy storage systems. Dielectric capacitors with high breakdown strength, energy usage efficiency and high energy power density have attracted attention due to their ability to be rapidly charged and discharged. These systems show very high-power densities, but fairly low energy densities meaning they are best suited to short-term high-power applications for example in pulsed power devices. Lead based ceramics have been used commercially for decades for a variety of applications such as actuators, sensors, transducers and capacitors.[1-2] Indeed, lead based antiferroelectrics (AFEs) such as $Pb_{0.98}La_{0.02}(Zr_{0.55}Sn_{0.45})_{0.995}O_5$ and $Pb_{0.97}La_{0.02}(Zr_{0.75}Sn_{0.20}Ti_{0.05})O_5$ show high energy storage properties.[3,4] However, the volatility and toxicity of lead have prompted legislation around the world restricting the use of lead based materials in electronic components.[5] Thus, there has been much research on development of lead-free ceramics with comparable properties to lead based systems.

Recently, there has been increased interest in bismuth sodium titanate ($Bi_{0.5}Na_{0.5}TiO_3$, BNT). Like Pb^{2+}, bismuth in its +3 oxidation state exhibits a $6s^2$ valence electron configuration and shows similar stereochemical activity of this valence electron pair. BNT adopts the perovskite structure and shows relaxor ferroelectric behaviour, with a depolarization temperature (T_d) of 196 °C and a temperature of maximum dielectric permittivity (T_m) of 330 °C.[6] BNT based materials are of interest as their high dielectric permittivity and low dielectric loss around T_m can be utilized for energy storage in capacitors, exhibiting higher power density than batteries. However, the T_m value of BNT is somewhat high for practical applications, which ideally would be in the range -60 °C to 180 °C. Much work has been carried out on lowering T_m by isovalent or aliovalent cation substitution, for example in the systems: $Bi_{0.5}Na_{0.5}TiO_3$-$SrTiO_3$,[7–9] $Bi_{0.5}Na_{0.5}TiO_3$-$BaTiO_3$,[10-11] $Bi_{0.5}Na_{0.5}TiO_3$-$Bi_{0.5}Na_{0.5}ZrO_3$ [12] and $Bi_{0.5}Na_{0.5}TiO_3$-$NaNbO_3$.[13] Barium titanate ($BaTiO_3$) is well known as a typical ferroelectric material, with high dielectric permittivity and exhibits three phase transitions: rhombohedral to orthorhombic at -80 °C, orthorhombic to tetragonal at 5 °C and tetragonal to cubic at the Curie point (T_c) of 120 °C.[14] Strontium titanate is reported to be a quantum paraelectric material with a Curie point near 0 K.[15] Substitution of

barium by strontium in $BaTiO_3$ has been found to lower T_c, for example $Ba_{0.4}Sr_{0.6}TiO_3$ (BST) exhibits a T_c of -60 °C.[16,17] Doping BNT with barium or strontium has been reported to lead to changes in T_m and T_d, with solid solutions showing morphotropic phase boundaries, associated with the coexistence of multiple ferroelectric phases.[18] The solid solution $(Bi_{0.5}Na_{0.5}TiO_3)_{1-x}(BaTiO_3)_x$ has been reported to be ferroelectric for $x \leq 0.06$ (*R*3*c*), relaxor antiferroelectric in the range $0.06 < x < 0.11$ (*P*4*bm*) and ferroelectric in the range $0.11 \leq x \leq 0.13$ (*P*4*mm*).[19] Strontium substitution in BNT, has been reported to result in lower T_m values and broaden its associated peak in dielectric permittivity over a large temperature range.[20]

The electrical behaviour in relaxor ferroelectrics has been explained in terms of the existence of polar nanoregions (PNRs).[21] The size and concentration of these PNRs directly influence the remnant polarization and the saturation polarization, which are key parameters dictating the energy density of capacitors. The switching dynamics of the PNRs is quite different to that in ferroelectric systems with large domains, leading to narrow polarization-electric field (PE) hysteresis loops, which are beneficial for energy efficiency due to low loss.

Our present work is aimed at shifting the T_d value of BNT to room temperature in order to achieve optimum performance for dielectric energy storage applications. We have examined double A-site substitution of Ba^{2+} and Sr^{2+} into BNT in the system $(Bi_{0.5}Na_{0.5}TiO_3)_{1-x}(Ba_{0.4}Sr_{0.6}TiO_3)_x$ (BST_xBNT_{1-x}) to investigate the effect on T_m as well as dielectric behaviour. Through optimisation of the polar structures in this system to achieve polar nanoregions a lowering of remnant polarization occurs leading to increased energy density.

2. Experimental

Samples of composition BST_xBNT_{1-x} (x = 0.0, 0.5, 0.8, 0.9, 1.0) were prepared using conventional solid synthesis. Pure BST and BNT powders were first prepared separately due to their different calcination temperatures. Stoichiometric amounts of the starting materials $BaCO_3$ (Aldrich, 99%), $SrCO_3$ (Aldrich, 99.9%) and TiO_2 (Aldrich, 99.8%) for BST or Bi_2O_3 (Aldrich, 99.9%) and Na_2CO_3 (Aldrich, 99.5%, preheated in an oven for 24 h at 200 °C) and TiO_2 for BNT were ground together in

ethanol, using a ball milling machine (QM-3SP4, Nanjing University Instrument Plant, China) for 4 h at 360 rpm (zirconia balls were used). The resulting slurry was dried and sieved using a 250 μm sieve. The BST and BNT powders were placed separately in alumina crucibles and calcined at 1000 °C for 2 h and 820 °C for 4 h, respectively. After calcination, the two powders were mixed according the required stoichiometry. In each case, the mixture was ball milled again for 4 h at 360 rpm in ethanol, dried and sieved using a 250 μm sieve. The mixture was pelletised using a small amount (ca. 2 ml) of a 5% w/w solution of polyvinyl acetate (PVA) in deionised water as a binder. Pellets of ca. 13 mm diameter and *ca*. 1 mm thickness were pressed uniaxially at a pressure of 150 MPa. The pellets were heated at 650 °C for 1 h to remove the PVA then for 3 h between 1150 and 1250 °C. The samples were then cooled in the furnace to room temperature over a period of *ca*. 12 h.

X-ray powder diffraction (XRD) data were collected on a PANAlytical X'Pert Pro diffractometer using Ni filtered Cu-Kα radiation (λ = 1.5418 Å). Data were collected at room temperature in flat plate θ/θ geometry over the 2θ range 5 -120°, with a step width of 0.0334° for 50 s per step. Powder neutron diffraction data were collected on the high-resolution powder diffractometer HRPD at the ISIS Facility, Rutherford Appleton Laboratory, UK. The sample was placed in an aluminium alloy slab geometry sample container with internal dimensions 18 × 23 mm perpendicular to the incident beam and 10 mm depth parallel to the beam. The sample was held between vanadium foil windows and all exposed Al and steel components of the cell were masked with Gd and Cd foils. Accurate and precise temperature control was achieved with a RhFe thermometer and a cartridge heater embedded in the sample holder frame, the latter working against the cooling power of ~ 50 mb of helium exchange gas chilled by a closed-cycle refrigerator (CCR) cold head. Data were collected at variable temperature from -263 °C to 150 °C; above 27 °C the exchange gas was completely evacuated from around the sample. Data acquired on the backscattering $158.46° < 2\theta < 176.11°$ bank, in the time of flight range 10-110 ms (0.22 to 2.22 Å) were used in subsequent analysis. X-ray and neutron data were modelled by Rietveld analysis using the GSAS-II suite of programmes.[22] Structure refinement was carried out in the cubic space groups *Pm*-3*m*.[23] Scanning electron microscopy (SEM, FEI Inspect-F Oxford) was used to examine the morphology of the sample surface.

For electrical measurements, pelletized samples were cut using a diamond saw to give approximate dimension 4 mm × 4 mm × 0.3 mm and polished using 2000 grade abrasive paper. The parallel surfaces were painted with silver paste and heated at (300 °C) to form conductive electrodes. The dielectric permittivity and loss were measured as a function of temperature using an LCR meter (Agilent 4284A) over the temperature range -195 °C to 160 °C. Ferroelectric current-electric field (I-E), polarization-electric field (P-E) and strain-electric field (S-E) loops were measured at room temperature using a ferroelectric hysteresis measurement tester (NPL, UK). The electric voltage was applied in a triangular waveform.[24]

3. Results and Discussion

Fig. 1a shows the X-ray powder diffraction patterns for the studied compositions, which reveal single phase cubic structures. The compositional variation of the lattice parameter is shown in Fig. 1b. A general expansion of the lattice with increasing *x*-value is seen as the average radius of the A site cations increases (Ba^{2+}:1.42, Sr^{2+}:1.26, Bi^{3+}:1.17 and Na^{1+}:1.18 Å, for the ions in 8 coordinate geometry).[25] SEM images (Fig. 2) confirm the compositions are highly crystalline, with well-defined cubic blocks with a grain size of *ca*. 1.5 μm.

The variation of relative dielectric permittivity (ε') and loss tangent (tan δ) for the studied compositions as a function of temperature at selected frequencies is shown in Fig. 3. For all compositions, broad dielectric permittivity and loss peaks are observed. The maximum dielectric permittivity shows frequency dependence, shifting to higher temperature at higher frequency, the extent of which decreases with increasing *x*-value, such that at $x = 1.0$ the peaks are virtually frequency independent. The T_m value is seen to decrease with increasing *x*-value and is consistent with previous reports on the ST-BNT system.[20] Both dielectric permittivity and loss decrease with increasing frequency below T_m and become frequency independent above T_m. This type of behaviour is a signature for relaxor ferroelectrics, where the dielectric permittivity peak occurs over a large temperature range and the peak temperature increases with frequency. In this case, The relaxor ferroelectric behaviour might be driven by the different valences or radii of

the A site cations as well as the Bi $6s^2$ lone pair configuration.[26,27] The dielectric relaxor behaviour for compositions of x = 0.5, 0.8 and 0.9 is consistent with the existence of polar nano regions (PNRs),[28] where the PNRs are randomly orientated within the bulk material, which results in an average non-polar structure. Double A-site substitution in the perovskite host structure of BNT, leads to an interruption of long-range order in the polar BNT phase, resulting in local ordering and the formation of PNRs.[9] In some BNT based materials, an additional transition temperature, T_s, is observed, corresponding to the transition between ferroelectric and relaxor ferroelectric phases.[29,30] The absence of a clear T_s in the doped compositions in present case is probably due to the lack of a clear structural transition (the structure remains cubic throughout the studied temperature range), i.e. the absence of a discrete FE to relaxor transition. The maximum permittivity peak associated with T_m is broad, which can be explained as resulting from a change in the size and dynamics of the polar regions, rather than being due to a phase transition.[31]

The dielectric permittivity at 100 kHz was analysed by a modified Curie-Weiss relationship, described by:

$$\frac{1}{\varepsilon} = \frac{1}{\varepsilon_m} + \frac{(T-T_m)^\gamma}{C} \quad (1)$$

where C is Curie Weiss constant and the exponent γ ($1 < \gamma < 2$) describes the extent of frequency dependence. Normal ferroelectric materials and ideal relaxor ferroelectric material have γ values of 1 and 2, respectively.[32] Fig. 4(a-c) shows fits to permittivity data for compositions x = 0.5 0.8 and 0.9. The resulting values of γ of around 1.5-1.7 are similar to those obtained for PZN-PT ($0.88PbZn_{0.33}Nb_{0.67}O_3 - 0.12PbTiO_3$, $\gamma = 1.58$), and PMN ($PbMg_{0.33}Nb_{0.67}O_3$, $\gamma = 1.64$), i.e. between a normal ferroelectric and an ideal relaxor material.[32] In addition, γ is seen to decrease with increasing x-value.

To better understand the relaxor behaviour of the studied compositions. The Vogel-Fulcher Law was applied as follows:

$$f = f_0 \exp[-E_a/k(T_m - T_{VF})] \quad (2)$$

where f is the frequency relative to the relaxation time, f_0 is the frequency at which the relaxor behaviour ceases, E_a is the activation energy for dipole reorientation, k is the Boltzmann constant and T_{VF} is the Vogel-Fulcher temperature corresponding to the

dipole freezing temperature[33]. Fig. 4(d-f) shows the frequency dependence of T_m (based on the dielectric permittivity data), with the solid line representing the best fit to the Vogel-Fulcher (VF) relationship. The values of T_{VF} are -18, -81 and -88 °C for compositions x = 0.5, 0.8 and 0.9, respectively.

Fig. 5 and Fig S3 show high field I-E/P-E loops for the studied compositions measured at room temperature compared to pure BNT. Pure BNT shows typical ferroelectric P-E loops with high remanent polarization and high coercive field, which lead to high total energy storage and low efficiency. The P-E loops observed for the x = 0.5 and 0.8 compositions are characteristic of relaxor-FEs with low values for P_r and E_c, ideal for energy storage applications. The value of saturation polarization P_s decreased with decreasing BNT content. For the x = 0.5 composition, four current peaks appear at around zero field via a field induced transitions related to PNRs giving rise to a higher saturation polarization.

Compared to normal ferroelectrics, which show higher P_r values and lower energy densities, the poor thermal stability of the PNRs in relaxor ferroelectrics make it difficult to achieve long-range order, leading to lower values of remnant polarization at temperatures above the dipole freezing temperature, T_f.

For a dielectric material the recoverable energy density W is given by:

$$W = \int_{P_r}^{P_s} E \, dP \tag{3}$$

where E is the electric field. The area in the PE loops therefore represents energy loss. Energy densities for the studied compositions are summarised in Table 1 and are compared to that for pure BNT. The maximum recoverable energy stored (1.618 J cm^{-3} at 17 kV mm^{-1}) was found for composition $BST_{0.5}BNT_{0.5}$, corresponding to 76.9% storage efficiency. In pure BNT, long-range FE ordering dominates leading to high remnant polarization, resulting in low energy density (0.072 J cm^{-3}) and hence low energy storage efficiency (2.9%). The co-substitution of Ba and Sr for Bi and Na in BNT leads to a reduction in the long-range ferroelectric ordering and enhances the concentration of PNRs. The concentration and dynamics of the PNRs are critical in determining the energy storage performance. High concentrations of PNRs, as in the x = 0.5 composition, can result in high saturation polarization and low remnant polarization, leading to higher energy density and efficiency than in pure BNT. When

the PNR concentration is reduced, as in the $x = 0.9$ composition, the total energy storage density is lowered due to the low saturation polarization.

Fig. S4 shows strain-electric field S-E loops for the studied compositions. In the undoped material, typical butterfly loops are observed which are attributed to non-180° domain switching. The $x = 0.5$ and 0.8 compositions show typical relaxor type S-E loops, with little hysteresis character and minima close to zero field.[34]

The Weibull distribution function was used to analyse the dielectric breakdown strength of the $x = 0.5$ composition.[35,36] The average breakdown strength is related to the probability of sample breakdown as follows:

$$P_i = 1 - exp(-\frac{E_i}{E_b})^{\beta} \quad (4)$$

$$P_i = \frac{i}{(n+1)} \quad (5)$$

where P_i is the breakdown probability of the ith sample, E_i is the measured breakdown strength for ith sample, measured using a ferroelectric tester, [37–39] and n is the total sample number. E_b is the calculated breakdown strength for 63.2% of samples to fail. Fig. S5 shows the fitted Weibull distribution of dielectric breakdown strength for the $x = 0.5$ composition. The average breakdown strength was found to be 17.28 kV mm^{-1}.

Fig. 6 shows selected temperature dependent P-E and I-E curves for the $x = 0.5$ composition over the electric field range ±4 kV mm^{-1} at 10 Hz. Data for other temperatures are given in Fig. S6. There is slight narrowing of the P-E loops with increasing temperature but other than this, little change is seen in the P-E loops up to 150 °C. The current peaks for the $x = 0.5$ composition are very broad at all measured temperatures. Two current peaks are evident at -75 °C and 125 °C, with four peaks at 25 °C. In BNT based materials, the electrical behaviour has been interpreted in terms of growth and dynamics of PNRs[9,40]. At low temperature (below T_f) the PNRs grow in size, but the dipoles become frozen and on switching at high electric field do not fully recover. This results in some remnant polarization after removal of the electric field i.e. an FE state. The remnant polarization increases on cooling as does the coercive field. At higher temperatures, the remnant polarization is reduced as the PNRs regain their switching dynamics. The observed field induced transition at room temperature is attributed to a weak-FE to strong-FE transition in the PNRs[9,40]. Further reduction of the

remnant polarization occurs at 75 °C accompanied by broad current peaks in the I-E loop. The fact that current peaks remain evident even at 150 °C indicates that the PNRs remain active up to at least this temperature.

In order to investigate the details of the pseudo-cubic structure, neutron diffraction experiments were carried out on the $x = 0.5$ composition. Fig. 7 shows high-resolution neutron diffraction patterns for this composition over the temperature range -263 °C to 150 °C. No peak splitting or additional peaks were observed, indicating the average cubic structure was maintained throughout the selected temperature range. The fitted neutron diffraction profiles at -263, 25 and 150 °C are shown in the electronic supporting information in Fig. S2, with crystal and refinement details summarised in Tables S1 and S2. The thermal evolution of unit cell volume on heating is shown in Fig. 8a. The data can be successfully fitted to a Debye type model (Fig. 8b, further details are given in the supporting information). The extent of thermal expansion increases gradually in the range -265 to -20 °C, above which temperature a linear thermal expansion is seen. This latter temperature agrees well with the freezing temperature (T_{VF} = -18 °C) obtained from the fit to the data in Fig. 4d. This type of behaviour is similar to that seen in the relaxor ferroelectric $PbMn_{0.33}Nb_{0.67}O_3$ (PMN), where the increasing thermal expansion was attributed to decreasing electrostriction associated with the decreasing root mean square of polarization.[41] Below T_{VF}, the PNRs become less active and stable dipoles are formed. This result is consistent with the variable temperature P-E results, where below T_{VF}, the two current peaks appear in the first and third quadrants in the I-E loop, while hysteresis increases in the P-E loop with a significant remnant polarization observed (Fig. 6).

Although the structure refinements give an average cubic structure, the existence of local polar nano-regions (PNRs) as indicated by the electrical data cannot be excluded. For example in the closely related strontium titanate-BNT system (ST-BNT), where the average structure is also cubic, PNRs have been observed by TEM and account for the observed electrical behaviour.[9] Revealingly, a plot of the thermal variation of the Gaussian peak variance parameter, σ_1^2, (which contains contributions from both sample and instrumental broadening) provides evidence for three distinct regions: -263 to -100 °C, -100 to 100 °C and 100 to 150 °C. Below -100 °C and above 100 °C the σ_1^2 value remains almost constant, but sharply increases between these

temperatures (Fig. 9). These two temperatures coincide with the start and end temperatures of the dielectric dispersion observed in Fig. 3. At low temperatures where the PNR concentration is high, but the dynamics are slow, as reflected by the low permittivity and frequency independence, there is a smaller range of atomic environments, variance of the Gaussian peak is low, and the Gaussian peak broadening is dominated by atomic thermal vibration. As the temperature is increased to around -100 °C, corresponding to the onset temperature of the frequency dispersion of the permittivity, the activity of the PNRs increases, leading to greater positional disorder and consequent peak broadening. This continues up to around *ca*. 100 °C, corresponding to the end of the frequency dispersion in the permittivity spectrum, where the PNR concentration is low. At this point, once again, increase in disorder is dictated by thermal vibration and the contribution from PNR activity is low. Microstrain shows an opposite trend to the Gaussian peak variance parameter (Fig. 9) and decreases with increasing temperature. At room temperature, the concentration of PNRs is high and as the material is cooled to -263 °C, the dynamics of the PNR rotation slow down and the lattice contracts. The combination of these two processes results in an increase in microstrain. On subsequent heating, the lattice expands and PNR rotation increases leading to a decrease in microstrain. Microstrain continues to decrease above ca. 100 °C, but at a slightly lower rate than in the range -100 to 100 °C, as the contribution from PNR activity becomes negligible.

At high temperature the concentration of PNRs is low and no dispersion is seen in the dielectric permittivity spectrum. On cooling from high temperature, the PNRs gradually increase in number and size, leading to an increase in dielectric permittivity. At 100 °C, there is a sufficient number of PNRs present to give rise to a dispersion in the spectrum. The frequency dependence of the dispersion is likely caused by PNRs of different sizes exhibiting a range of activation energies for dielectric response. On further decreasing the temperature, the dipoles in the PNRs gradually loose activity due to the freezing effect, the start of which occurs at T_{VF} and results in a weakening dielectric dispersion. Eventually, at -100 °C, the dipoles in the PNRs become inactive, with the dielectric permittivity becoming frequency independent.

4. Conclusions

Compositions of BST_xBNT_{1-x} were successfully synthesised by solid state methods. All the samples exhibited single phase perovskite type structures. The $x = 0.5$ composition exhibited a cubic perovskite structure in space group *Pm*-3*m*. There is little variation of this average structure with temperature over the range -263 to 150 °C. However, electrical measurements confirm this composition exhibits relaxor ferroelectric behaviour, consistent with the existence of PNRs. The activity of these PNRs is associated with a frequency dependent dispersion in the temperature range -100 to 100°C. Interestingly, this activity manifests itself structurally with changes in microstrain, the thermal evolution of which can readily be followed through changes in the Gaussian variance peak shape parameter. The thermal variation of lattice parameter shows curvature at low temperatures becoming linear at high temperatures; the onset of the linear range corresponding to the dipole freezing temperature T_f in good agreement with values derived from fitting the maximum permittivity values using the Vogel-Fulcher Law.

At $x = 0.5$ two different field induced transitions are observed at room temperature associated with a field induced transition between weak polar and strong polar phases in the PNRs. A maximum recoverable energy storage density of 1.618 J cm^{-3} with 76.9% efficiency was found for composition $BST_{0.5}BNT_{0.5}$, which makes it a potential candidate for energy storage applications.

5. Acknowledgements

The authors are grateful to the Materials Research Institute at Queen Mary for studentship funding for Hangfeng Zhang. The authors gratefully acknowledge a neutron beam time award (RB1620158) at the STFC ISIS Facility.

6. References

1 X. Hao, *J. Adv. Dielectr.*, 2013, **03**, 1330001.

2 A. Chauhan, S. Patel, R. Vaish and C. R. Bowen, *Materials (Basel).*, 2015, **8**, 8009–8031.

3 H. Wang, Y. Liu, T. Yang and S. Zhang, *Adv. Funct. Mater.*, 2019, **29**, 1807321.

4 X. Hao, J. Zhai, L. B. Kong and Z. Xu, *Prog. Mater. Sci.*, 2014, **63**, 1–57.

5 J. Rödel, W. Jo, K. T. P. Seifert, E. Anton, T. Granzow and D. Damjanovic, *J. Am. Ceram. Soc.*, 2009, **92**, 1153–1177.

6 Y. Hiruma, H. Nagata, T. Takenaka, Y. Hiruma, H. Nagata and T. Takenaka, *J. Appl. Phys.*, 2009, **105**, 084112.

7 Y. Hiruma, Y. Imai, Y. Watanabe, H. Nagata and T. Takenaka, *Appl. Phys. Lett.*, 2008, **92**, 262904.

8 K. Sakata and Y. Masuda, *Ferroelectrics*, 1974, **7**, 347–349.

9 J. Wu, A. Mahajan, L. Riekehr, H. Zhang, B. Yang, N. Meng, Z. Zhang and H. Yan, *Nano Energy*, 2018, **50**, 723–732.

10 M. Chandrasekhar and P. Kumar, *Ceram. Int.*, 2015, **41**, 5574–5580.

11 Y. Yao, Z. Luo and Y. Yang, *Acta Mater.*, 2016, **103**, 746–753.

12 B. K. Barick, R. N. P. Choudhary and D. K. Pradhan, *Ceram. Int.*, 2013, **39**, 5695–5704.

13 Q. Xu, Z. Song, W. Tang, H. Hao, L. Zhang, M. Appiah, M. Cao, Z. Yao, Z. He and H. Liu, *J. Am. Ceram. Soc.*, 2015, **98**, 3119–3126.

14 A. Von Hippel, *Rev. Mod. Phys.*, 1950, **22**, 221–237.

15 K. A. Müller and H. Burkard, *Phys. Rev. B*, 1979, **19**, 3593–3602.

16 L. Zhou, P. M. Vilarinho and J. L. Baptista, *J. Eur. Ceram. Soc.*, 1999, **19**, 2015–2020.

17 H. Zhang, H. Giddens, Y. Yue, X. Xu, V. Araullo-Peters, V. Koval, M. Palma, I. Abrahams, H. Yan and Y. Hao, *J. Eur. Ceram. Soc.*, 2020, **40**, 3996–4003.

18 C. Ma and X. Tan, *Solid State Commun.*, 2010, **150**, 1497–1500.

19 R. Garg, B. N. Rao, A. Senyshyn, P. S. R. Krishna and R. Ranjan, *Phys. Rev. B*, 2013, **88**, 014103.

20 J. R. Gomah-Pettry, a. N. Salak, P. Marchet, V. M. Ferreira and J. P. Mercurio,

Phys. Status Solidi, 2004, **241**, 1949–1956.

21 D. Viehland, S. J. Jang, L. E. Cross and M. Wuttig, *J. Appl. Phys.*, 1990, **68**, 2916–2921.

22 B. H. Toby and R. B. Von Dreele, *J. Appl. Crystallogr.*, 2013, **46**, 544–549.

23 J. H. G.M. Meyer, R.J. Nelmes, *Ferroelectrics*, 1978, **21**, 461.

24 G. Viola, T. Saunders, X. Wei, K. B. Chong, H. Luo, M. J. Reece and H. Yan, *J. Adv. Dielectr.*, 2013, **03**, 1350007.

25 R. D. Shannon, *Acta Crystallogr.*, 1976, **32**, 751–767.

26 V. V. Shvartsman and D. C. Lupascu, *J. Am. Ceram. Soc.*, 2012, **95**, 1–26.

27 A. A. Bokov, *Ferroelectrics*, 1992, **131**, 49–55.

28 G. Viola, Y. Tan, R. A. McKinnon, X. Wei, H. Yan and M. J. Reece, *Appl. Phys. Lett.*, 2014, **105**, 102906.

29 T. Li, C. Liu, X. Ke, X. Liu, L. He, P. Shi, X. Ren, Y. Wang and X. Lou, *Acta Mater.*, 2020, **182**, 39–46.

30 X. Liu, Y. Zhao, J. Shi, H. Du, X. Xu, H. Lu, J. Che and X. Li, *J. Alloys Compd.*, 2019, **799**, 231–238.

31 K. Roleder, A. Kania and J. Handerek, *Ferroelectrics*, 1988, **77**, 107–110.

32 K. Uchino and S. Nomura, *Ferroelectrics*, 1982, **44**, 55–61.

33 G. A. Samara, *J. Phys. Condens. Matter*, 2003, **15**, R367–R411.

34 G. H. Haertling, *Ferroelectr. Fundam. Collect.*, 2007, **818**, 157–178.

35 Z. Yan, D. Zhang, X. Zhou, H. Qi, H. Luo, K. Zhou, I. Abrahams and H. Yan, *J. Mater. Chem. A*, 2019, **7**, 10702–10711.

36 L. Zhao, Q. Liu, J. Gao, S. Zhang and J. F. Li, *Adv. Mater.*, 2017, **29**, 1–7.

37 D. Zhang, X. Zhou, J. Roscow, K. Zhou, L. Wang, H. Luo and C. R. Bowen, *Sci. Rep.*, 2017, **7**, 1–11.

38 H. Luo, J. Roscow, X. Zhou, S. Chen, X. Han, K. Zhou, D. Zhang and C. R. Bowen, *J. Mater. Chem. A*, 2017, **5**, 7091–7102.

39 N. Meng, X. Ren, G. Santagiuliana, L. Ventura, H. Zhang, J. Wu, H. Yan, M. J. Reece and E. Bilotti, *Nat. Commun.*, 2019, **10**, 4535.

40 C. Ma, H. Guo, S. P. Beckman and X. Tan, *Phys. Rev. Lett.*, 2012, **109**, 107602.

41 P. Bonneau, P. Garnier, G. Calvarin, E. Husson, J. R. Gavarri, A. W. Hewat and A. Morell, *J. Solid State Chem.*, 1991, **91**, 350–361.

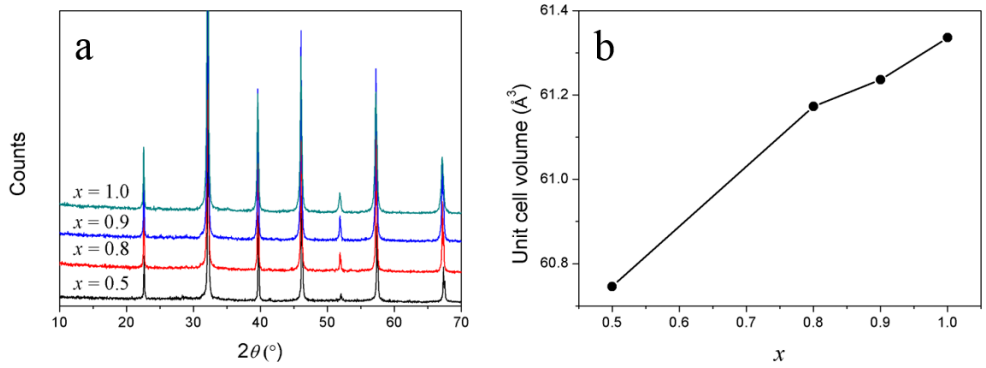

Fig. 1 (a) X-ray powder diffraction patterns and (b) compositional variation of cubic lattice parameter in the BST_xBNT_{1-x} system. Error bars are smaller than the symbols used.

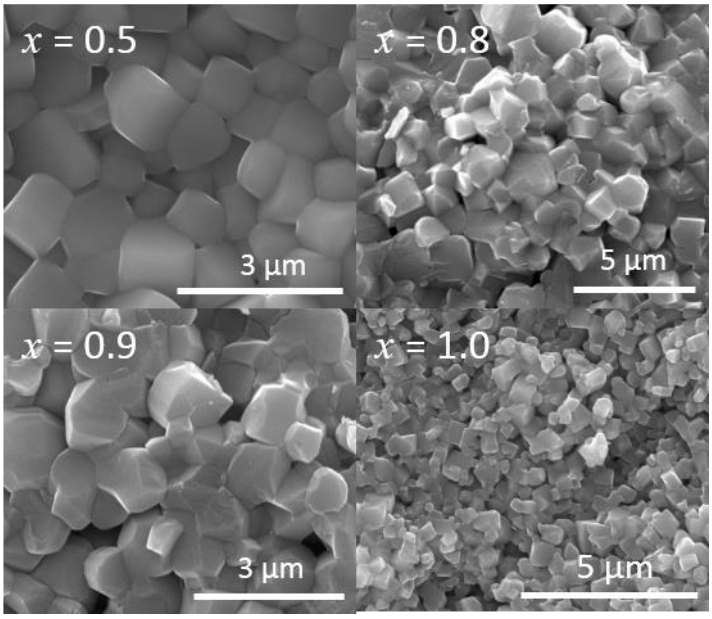

Fig. 2. SEM images of BST_xBNT_{1-x} ceramics.

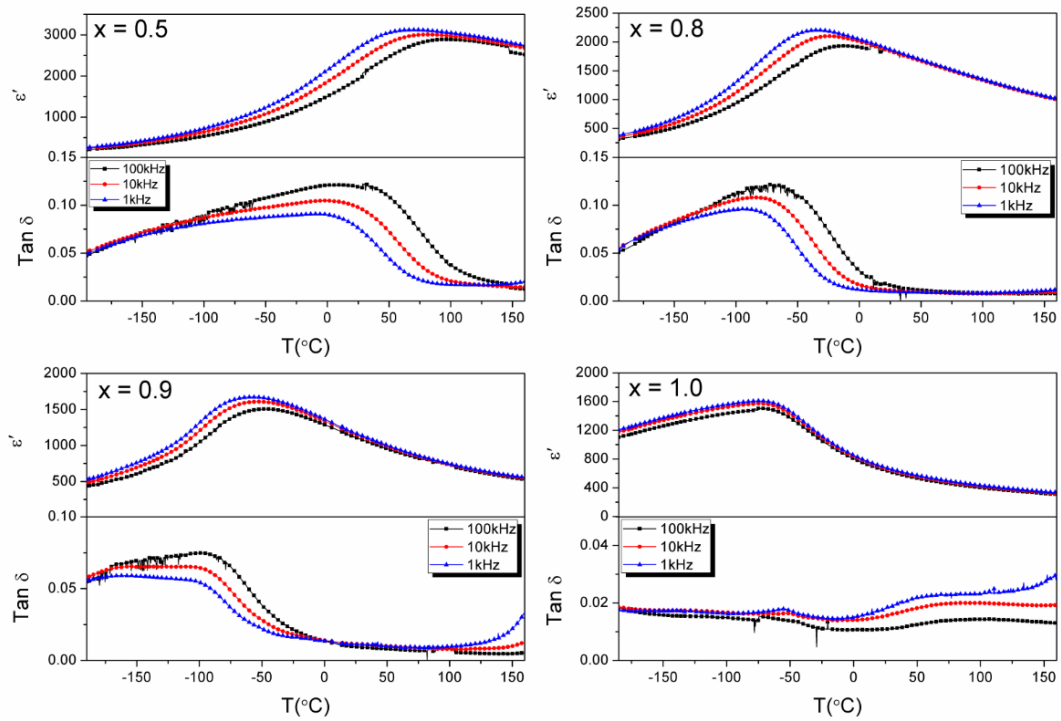

Fig.3. Temperature dependence of dielecric permittivity and loss for BST_xBNT_{1-x}.

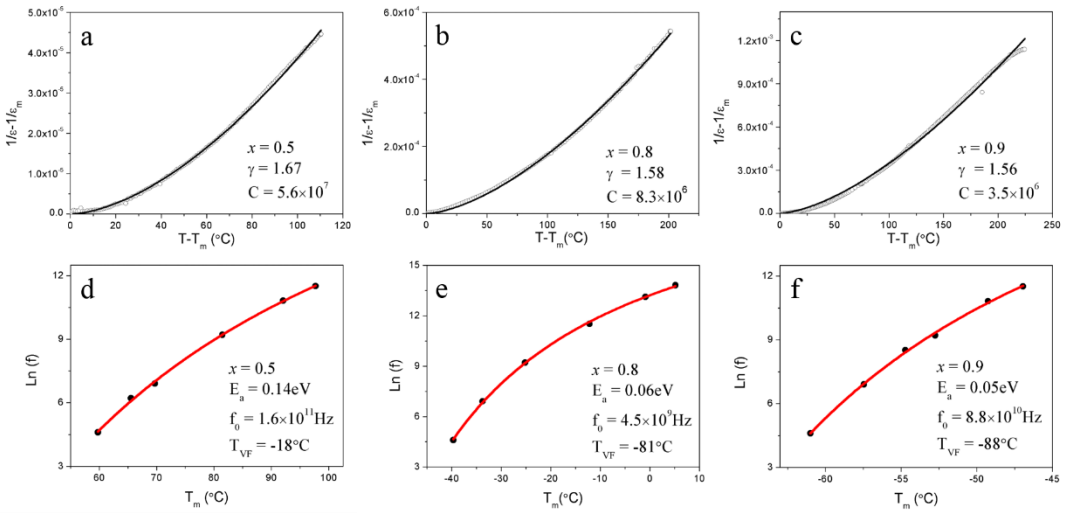

Fig. 4. (a-c) Fits to dielectric permittivity data for BST_xBNT_{1-x} (x = 0.5 to 0.9) using the modified Curie-Weiss law. (d-f) Vogel-Fulcher fits for BST_xBNT_{1-x} (x = 0.5 to 0.9).

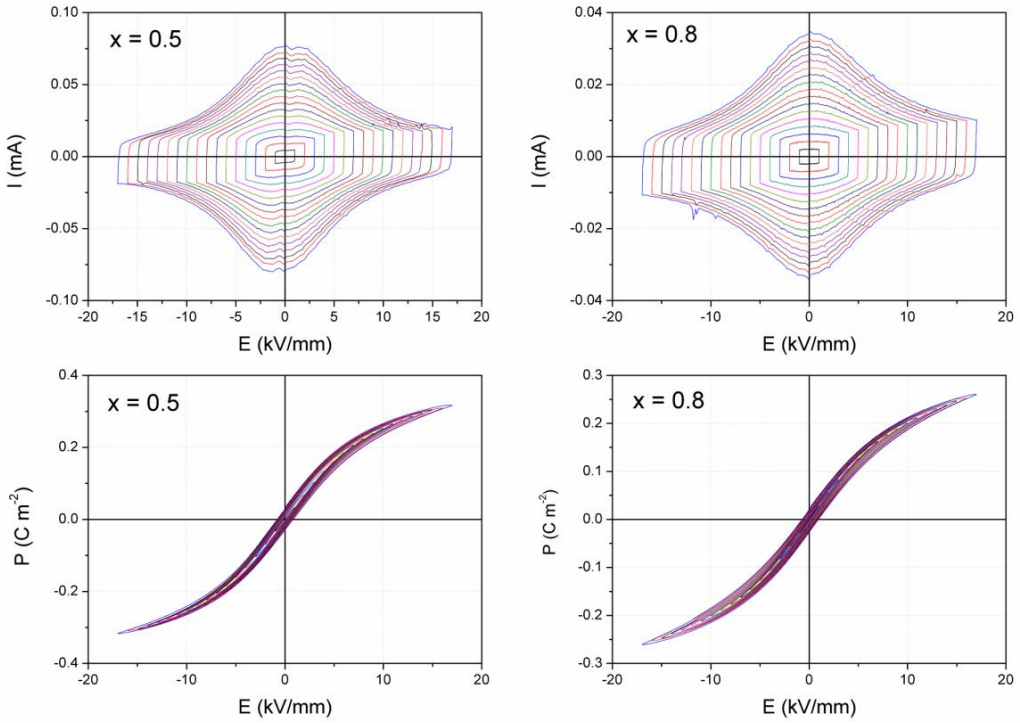

Fig. 5. High field I-E/P-E loops of studied compositions at room temperature.

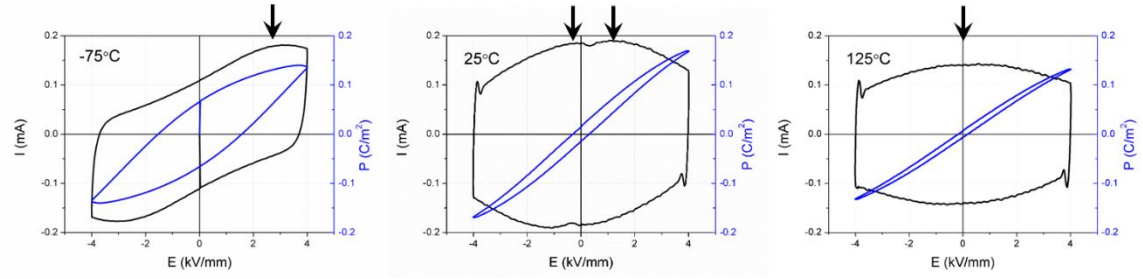

Fig. 6. PE/IE loops at selected temperatures for $BST_{0.5}BNT_{0.5}$.

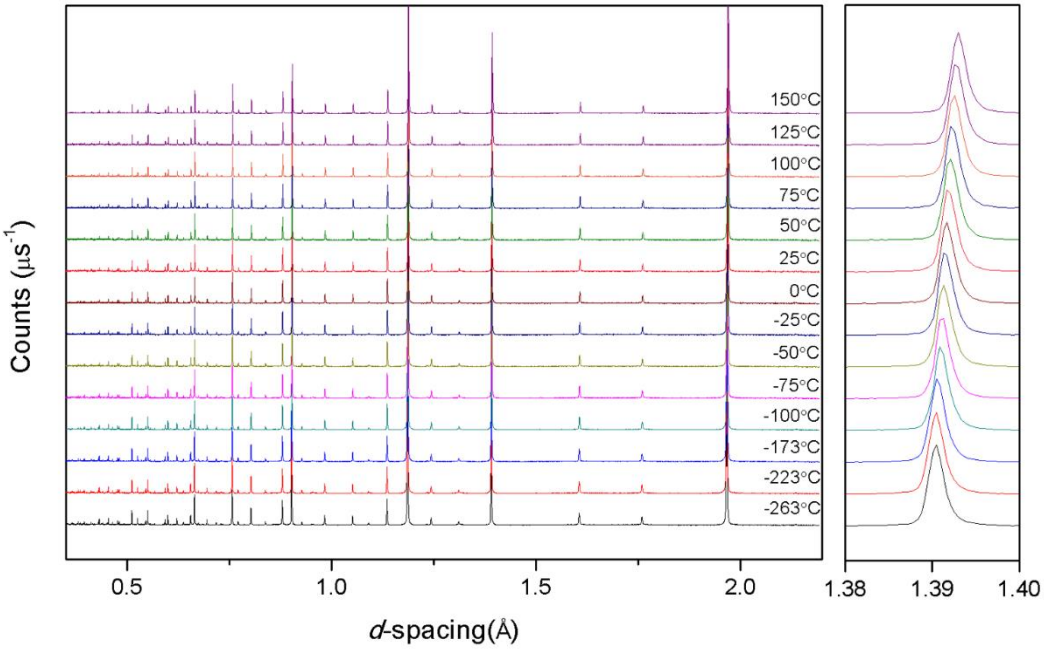

Fig. 7. Variable temperature of neutron diffraction patterns for $BST_{0.5}BNT_{0.5}$.

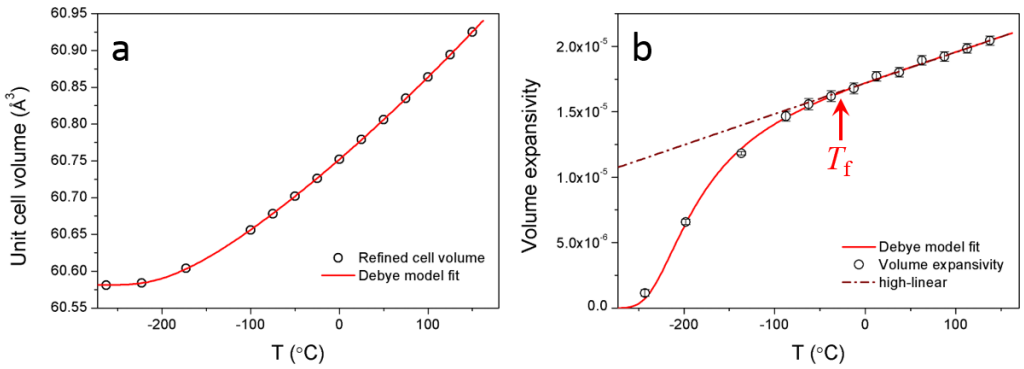

Fig. 8. (a) Thermal variation of unit cell volume for $BST_{0.5}BNT_{0.5}$ derived from neutron diffraction data and (b) Debye model fitting for volume expansion.

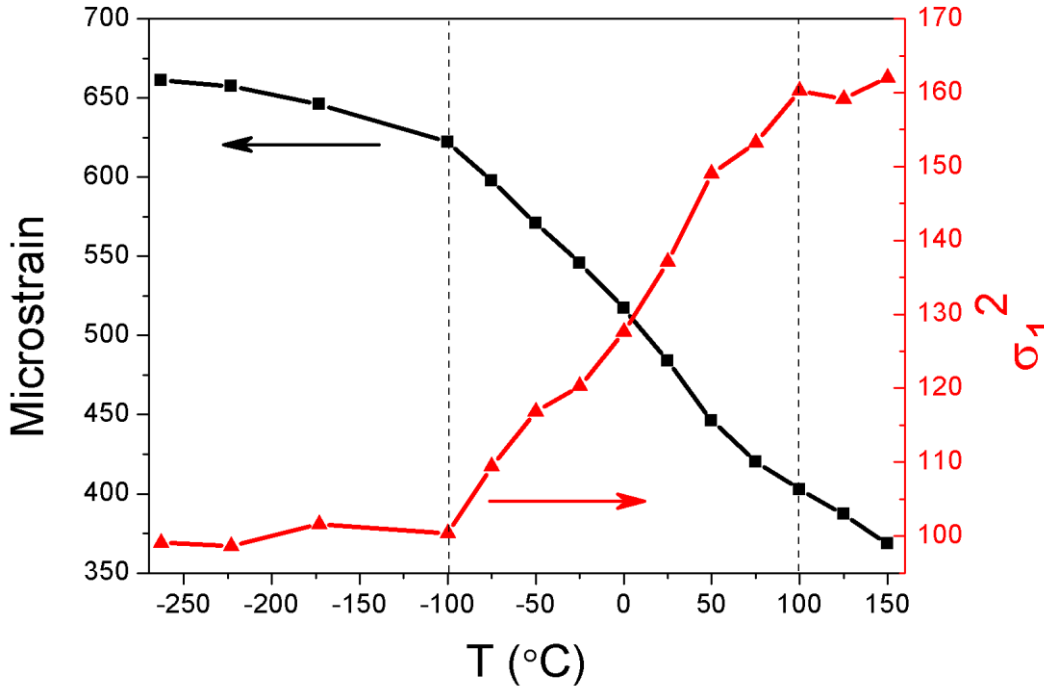

Fig. 9. Thermal dependence of microstrain and Gaussian peak variance function in $BNT_{0.5}BST_{0.5}$

Table 1. Energy density values obtained from high field P-E loops (Fig. 5 and S3)

x	Recoverable energy (J cm^{-3})	Energy loss (J cm^{-3})	Total charging energy (J cm^{-3})	Applied Electric field (kV mm^{-1})	Energy efficiency (%)
0.0	0.072	2.372	2.444	9	2.9
0.5	1.618	0.486	2.104	17	76.9
0.8	1.468	0.413	1.881	17	78.0
0.9	0.738	0.236	0.974	18	75.8
1.0	0.681	0.149	0.830	18	82.0